RESEARCH ARTICLE

Key Points:
- Global MHD simulation of extreme Carrington-type space weather event
- Discuss reaction of magnetosphere-ionosphere system to extreme driving
- Provide results off extreme geomagnetically induced electric fields

Correspondence to:
C. M. Ngwira,
chigongwira@yahoo.co.uk

Modeling extreme "Carrington-type" space weather events using three-dimensional global MHD simulations

Chigomezyo M. Ngwira[1,2], Antti Pulkkinen[2], Maria M. Kuznetsova[2], and Alex Glocer[2]

[1]Department of Physics, Catholic University of America, Washington, District of Columbia, USA, [2]NASA Goddard Space Flight Center, Space Weather Laboratory, Greenbelt, Maryland, USA

Abstract There is a growing concern over possible severe societal consequences related to adverse space weather impacts on man-made technological infrastructure. In the last two decades, significant progress has been made toward the first-principles modeling of space weather events, and three-dimensional (3-D) global magnetohydrodynamics (MHD) models have been at the forefront of this transition, thereby playing a critical role in advancing our understanding of space weather. However, the modeling of extreme space weather events is still a major challenge even for the modern global MHD models. In this study, we introduce a specially adapted University of Michigan 3-D global MHD model for simulating extreme space weather events with a *Dst* footprint comparable to the Carrington superstorm of September 1859 based on the estimate by Tsurutani et. al., (2003). Results are presented for a simulation run with "very extreme" constructed/idealized solar wind boundary conditions driving the magnetosphere. In particular, we describe the reaction of the magnetosphere-ionosphere system and the associated induced geoelectric field on the ground to such extreme driving conditions. The model setup is further tested using input data for an observed space weather event of Halloween storm October 2003 to verify the MHD model consistence and to draw additional guidance for future work. This extreme space weather MHD model setup is designed specifically for practical application to the modeling of extreme geomagnetically induced electric fields, which can drive large currents in ground-based conductor systems such as power transmission grids. Therefore, our ultimate goal is to explore the level of geoelectric fields that can be induced from an assumed storm of the reported magnitude, i.e., *Dst* $\sim= -1600$ nT.

1. Introduction

Solar activity such as coronal mass ejections (CMEs) are the main drivers of the most severe (or "extreme") space weather events [e.g., *Gopalswamy et al.*, 2005b]. Space weather is a major concern for modern-day society because of its adverse impacts on technological infrastructure such as electrical power grids, oil pipelines, and global navigation systems. The threat of severe societal consequences has prompted renewed interest to further our understanding of extreme space weather and geomagnetic storm events [see e.g., *Thomson et al.*, 2011; *Pulkkinen et al.*, 2012; *Ngwira et al.*, 2013a, 2013b, and references therein]. The ultimate challenge for the scientific community is to develop innovative tools to more accurately predict these extreme space weather events.

The coupling of fast moving CMEs to planetary magnetospheres has been a subject of great scientific interest [e.g., *Weimer*, 1996; *Groth et al.*, 2000; *Wang et al.*, 2008; *Pulkkinen et al.*, 2010; *Ngwira et al.*, 2013b, and references therein]. The magnetosphere is a highly complex nonlinear system whose large-scale state is controlled primarily by the orientation of the interplanetary magnetic field (IMF) and solar wind plasma properties. The transfer of mass, momentum, and energy from the solar wind into the magnetosphere-ionosphere system produces various transition layers, the extended geomagnetic tail, and different dynamic current systems and auroral processes.

Three-dimensional (3-D) global magnetohydrodynamics (MHD) models play a critical role in simulating the large-scale dynamics of magnetospheric plasmas. These first principles physics-based models represent a very important component of attempts to understand the response of the magnetosphere-ionosphere system to varying solar wind conditions [see, e.g., *Gombosi et al.*, 2000; *Palmroth et al.*, 2004; *Manchester et al.*, 2006; *Kuznetsova et al.*, 2007]. Some of these studies include the following: the global magnetic field configuration [e.g., *Welling and Ridley*, 2010], reconnection at the dayside magnetopause and in the magnetotail [e.g., *Kuznetsova et al.*, 2007], the dependence of magnetospheric convection on the IMF orientation

[e.g., *Ridley et al.*, 1998], and variations in the magnetosheath during storm main phase [e.g., *Kataoka et al.*, 2005]. Upstream solar wind parameters are used as driving conditions for many simulation models of the magnetosphere-ionosphere system, and the results (or performance of these models) are validated by comparing with ground-based or satellite observations [*Palmroth et al.*, 2003; *Pulkkinen et al.*, 2010; *Welling and Ridley*, 2010; *Pulkkinen et al.*, 2013].

Understanding of the magnetosphere and ionosphere dynamics during extreme solar wind driving is still a major challenge mainly because of lack of modern scientific data from such periods [see, e.g., *Ridley et al.*, 2006]. It is generally agreed within the space weather community that the Carrington superstorm of 1–2 September 1859 is the most extreme geomagnetic storm on record, and therefore, it presents a special opportunity to study extreme space weather. Obviously, no upstream solar wind measurements were available at that time. However, *Tsurutani et al.* [2003] published ground-based magnetogram observations recorded during the Carrington superstorm at Colaba, India (∼9.81°N, 143.4°E, geomagnetic). There are several other magnetic recordings of the Carrington superstorm including high-latitude observations; however, to our knowledge, all of these recordings went off scale during the peak of the storm [see, e.g., *Nevanlinna*, 2008; *Cliver and Dietrich*, 2013, and references therein]. Consequently, attempts to model the Carrington event can be linked with the Colaba ground-based magnetic field observations. From the manually recorded magnetograms, *Tsurutani et al.* [2003] estimated the minimum negative intensity of the horizontal geomagnetic field (*H* component) at Colaba to have been about −1600 nT.

In the present study, we use the estimated minimum negative geomagnetic intensity as a benchmark for our simulations. We present a global 3-D MHD model with specially refined settings for simulating space weather events that are constructed using extreme upstream solar wind input conditions. Historically, MHD models have typically been utilized for studying nonextreme events. So the primary purpose of this paper is to examine the response of the simulated magnetosphere-ionosphere coupled system, and the ground geomagnetic and geoelectric fields during extreme solar wind driving conditions. Modeling such extreme conditions represents a major challenge even for modern global MHD models.

In section 2, we highlight the basic details of the global MHD and geoelectric field modeling approaches specific to this study. In section 2.1 we first briefly describe the general MHD modeling framework, the framework domains used and the coupling between these domains. Then, in section 2.2, we present the various refinements in the model setting that have been introduced in order to accommodate very extreme space weather driving conditions. Section 2.3 outlines the geomagnetic and geoelectric field modeling process. The solar wind scenario used in this study is described in section 3, while the simulation results are provided and discussed in section 4. A summary and conclusions to this work is contained in section 5.

2. Description of the Modeling Approach

2.1. The Space Weather Modeling Framework

The core of the simulation process presented in this paper is the University of Michigan Space Weather Modeling Framework (SWMF). The SWMF is a flexible framework that integrates various physics-based numerical models into a high-performance coupled model via a standardized interface and a highly efficient parallel coupling toolkit [*Tóth et al.*, 2005, 2012]. The SWMF creates an environment where simulations that were impossible with individual physics models can be performed.

The SWMF predicts in a self-consistent manner the dynamic response of the large-scale magnetospheric plasma to changing solar wind conditions using the block-adaptive tree solar wind Roe-type upwind scheme (BATSRUS) global MHD code [*Powell et al.*, 1999; *Gombosi et al.*, 2000]. The BATSRUS code uses a block-adaptive mesh with either cartesian or generalized coordinates basic structure that partitions space into regions, each of which is a regular grid of cells. The blocks in the grid, at their various levels of refinement, are stored in a tree-like data structure. A detailed description of the University of Michigan MHD code can be found in reports by *Powell et al.* [1999] and *Groth et al.* [1999], whereas the core design and implementation of the SWMF is fully described by *Tóth et al.* [2012]; therefore, only the basic SWMF domains that are most relevant for the study outlined in this paper are described below.

In the Global Magnetosphere (GM) domain, the upstream boundary conditions are derived from the Inner Heliosphere component or from in situ satellite observations. In the present work, the GM component is driven by specially tailored solar wind scenarios, which are described in section 3. The physics of the GM component is approximated with resistive MHD equations except near the inner boundary where it overlaps

with the inner magnetosphere. The resistivity is determined by the numerics in the simulation. Additionally, the GM component inner boundary conditions are partly derived from the Ionospheric Electrodynamics (IE) component, which makes available the electric potentials.

Coupling of the GM component to the Inner Magnetosphere (IM) component is achieved through the Rice Convection Model (RCM) [*De Zeeuw et al.*, 2004], which is a massive numerical computation code developed at Rice University. The code offers a description of the coupled inner magnetosphere-ionosphere system electrodynamics. The RCM is a kinetic model that solves time-dependent coupled equations describing plasma motion in the inner magnetosphere, and self-consistently computes field-aligned currents (FACs) and ionospheric potentials using provided magnetic field inputs [*Toffoletto et al.*, 2003; *De Zeeuw et al.*, 2004]. It should be noted that single fluid isotropic MHD cannot produce realistic ring current, which is central feature of the inner magnetosphere. Plasma information about the closed field lines required by the IM component are obtained from the GM component, and in return the IM provides the density and pressure corrections along the closed field lines to the GM component [*Tóth et al.*, 2005].

For solar wind-magnetosphere interaction modeling, it is important to take also the coupling between the magnetosphere and ionosphere into account. The ionosphere allows closure of magnetospheric currents, which is required for realistic magnetospheric convection to occur [e.g., *Fedder et al.*, 1998]. The SWMF carries out this process through the IE domain in which it is assumed that magnetospheric FACs can penetrate into a height-integrated electrostatic ionosphere. *Ridley et al.* [2004] thoroughly explains the coupling between the magnetosphere and ionosphere in the MHD code. The IE domain is a 2-D height-integrated spherical surface that can be described by several mathematical models including the following: empirical models for electric potential, particle precipitation and auroral conductance maps [e.g., *Fuller-Rowell and Evans*, 1987; *Weimer*, 1996], and/or a height-averaged electric potential solver [e.g., *Ridley et al.*, 2004]. The auroral precipitation pattern used by the IE component are determined from FACs that are in turn obtained from the GM component and upper atmosphere [*Tóth et al.*, 2005]. The IE component in the current version of the SWMF utilizes a potential solver and Hall and Pedersen conductance generated by auroral pattern and solar illumination.

2.2. Refined Grid Structure

The magnetosphere cavity was simulated in a computational box defined by dimensions $-224\, R_E < x < 32\, R_E$, $-128\, R_E < y < 128\, R_E$, and $-128\, R_E < z < 128\, R_E$ where R_E is Earth radii, with the Earth placed at the center. The dipole tilt in the simulation is set to update throughout each run so that it is dependent on the day of the year and the time of the day. The simulations were carried out using a block-adaptive high-resolution grid with minimum cell size of $1/16\, R_E$ and with about 8.9 million computational cells. A high-resolution grid is required here because it is better suited to resolve the rapid and/or large changes at the magnetopause that are introduced by the extreme solar wind conditions [*Ridley et al.*, 2010].

Specifically for our simulations, magnetosphere currents were mapped at $1.5\, R_E$ from the center of the Earth, while the BATSRUS MHD model inner boundary sphere is set at $1.25\, R_E$ (usually set at $2.5\, R_E$ for "normal" simulations). The BATSRUS inner boundary sphere is connected to the electrostatic ionosphere, represented by a height-integrated potential solver [*De Zeeuw et al.*, 2004; *Ridley et al.*, 2004], at a high coupling rate initiated every 15 s. This is desired for space weather applications such as the study of geomagnetically induced currents (GIC) in order to capture rapidly varying ionospheric currents that generate large-amplitude geoelectric fields. A sunspot number with a value of 110 related to the Carrington storm was used, and an auroral conductance (realistic oval) driven by FACs and a solar EUV component with an solar flux $F_{10.7}$ value of 275 SFU or solar flux units (1 SFU = 10^{-22} W m^{-2} Hz^{-1}). This value of $F_{10.7}$ is consistent with solar maximum conditions. Because of the high inner magnetosphere coupling rate (15 s), in combination with the very compact and computationally expensive grid, each simulation required a substantial amount of computational resources. Thus, in this initial study we had to restrict runs to 4 h of length in physical time.

2.3. Geomagnetic and Geoelectric Field Modeling

In SWMF the ground magnetic perturbations are computed by summing over all the magnetospheric, ionospheric and gap region current systems within the near-Earth space environment using a Biot-Savart integral [see, e.g., *Yu et al.*, 2010]. In addition, the ring current dynamics are simulated in a realistic fashion using the RCM coupled to BATSRUS. However, single fluid MHD modeling cannot provide adequate description of the inner magnetosphere, and thereby, our approach does not capture all possible dynamic processes that drive large currents (i.e., auroral substorms and equatorial electrojet or EEJ) in the auroral and

equatorial zones, respectively [see, e.g., *De Zeeuw et al.*, 2004]. We cannot expect to reproduce EEJ at all since the physics is missing in the model. However, a more detailed discussion on the topic of auroral dynamics is provided in section 4.3 below. Furthermore, the modeled *Dst* index is also calculated by solving the Biot-Savart integral for all the electric currents within the BATSRUS simulation domain, including the RCM, from the inner boundary outward, and taking the magnetic field disturbance along the *z* axis at the center of the coordinate system.

The evaluation of SWMF/BATSRUS simulation performance is widely documented [see, e.g., *Groth et al.*, 1999; *Pulkkinen et al.*, 2009; *Yu et al.*, 2010; *Welling and Ridley*, 2010; *Pulkkinen et al.*, 2013, and references therein]. For example, *Pulkkinen et al.* [2009] showed that the GIC computed from model-derived geomagnetic field perturbations can be slightly overestimated but are generally comparable to the GIC computed from ground magnetometer observations. Additionally, *Yu et al.* [2010] demonstrates that SWMF-generated ground perturbations can be more accurately modeled by inclusion of magnetospheric driven current systems within the near-Earth space environment. This is all consistent with work by *Pulkkinen et al.* [2011] that illustrates that increasing the global SWMF spatial resolution and the inclusion of the ring current dynamics improves the SWMF capability to generate more realistic ground magnetic field fluctuations.

From the SWMF-generated ground magnetic perturbations, we calculated the geoelectric fields using the plane wave method [see, e.g., *Cagniard*, 1953; *Pirjola*, 1982]. The model generates magnetic field perturbations at locations of 130 active International Real-time Magnetic Observatory Network (INTERMAGNET, www.intermagnet.org) magnetometer sites. Then, the geoelectric field components $E_{x,y}$ can be computed in terms of the perpendicular geomagnetic field components $B_{y,x}$ as

$$E_{x,y} = \pm \frac{1}{\sqrt{\pi \mu_0 \sigma}} \int_{-\infty}^{t} \frac{1}{\sqrt{t-u}} \frac{dB_{y,x}(u)}{dt} \, du \tag{1}$$

where μ_0 is the permeability of free space and σ is the effective conductivity. For a nonuniform Earth composing of horizontal layers, σ takes the role of an apparent conductivity that is dependent on the frequency reflecting the penetration depth of the electric and magnetic fields into the Earth [*Pirjola*, 2002]. The resistive-end Quebec multilayer ground conductivity model was applied [see *Pulkkinen et al.*, 2012], since our interest is in extreme event cases. Strictly speaking, the standard plane wave method is not directly applicable here, because the method assumes that the ground magnetic field signal includes both external and internal contributions. However, this will not introduce significant errors in the modeled geoelectric fields because the internal contribution is relatively small compared to the external, as explained by *Ngwira et al.* [2013b].

3. Solar Wind Input Parameters

Following *Tsurutani et al.* [2003] report, *Li et al.* [2005] and *Manchester et al.* [2006] demonstrated that a Carrington-type event has to be associated with very extreme solar wind driving conditions. *Li et al.* [2005] using an updated empirical *Dst* prediction model were able to closely reproduce the Colaba magnetogram ground signature using estimated solar wind conditions. To capture the fast recovery of the Carrington storm, they introduced an exceptionally large density pulse ($\sim$1800 cm^{-3}) after the negative B_z phase. In their paper, *Manchester et al.* [2006] present a CME simulation model designed to reproduce the short Sun-Earth transit time of the Carrington event and the solar wind parameters at 1 astronomical unit (1 AU). Also, their model results yielded an extremely large density ($\sim$800 cm^{-3}) and equally large IMF Bz component with a minimum around -200 nT.

The solar wind data published by *Li et al.* [2005] and *Manchester et al.* [2006] provided a general guideline for construction of our synthetic solar wind data. All the solar wind parameters were artificially/manually estimated initially, and then the final data sets used in our simulations were derived by superposing observed events, i.e., a portion of the Halloween 2003 storm, on the synthetically constructed solar wind conditions. The reason for doing this was to introduce realistic solar wind fluctuations at approximately the same temporal scale as for previously observed events. We learned that this is important for introducing balancing fluctuations in the magnetospheric structures that under extreme driving conditions could otherwise become numerically unstable and produce unrealistic features in the simulations.

Here we attempted to reproduce as close as possible the minimum geomagnetic perturbation of -1600 nT. This value is unprecedented at the latitude of the Colaba station [see, e.g., *Siscoe et al.*, 2006], thus represents
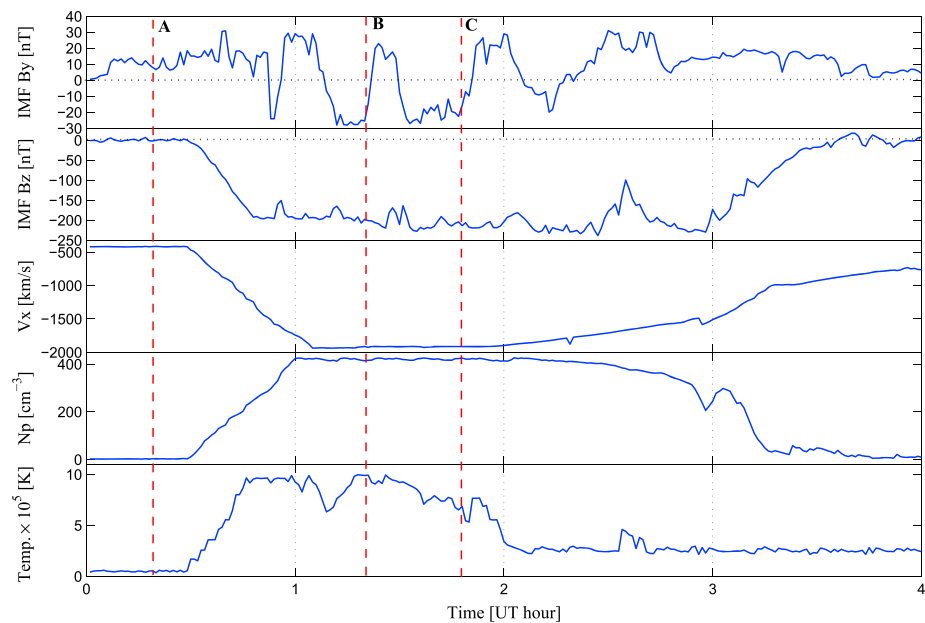
Figure 1. Interplanetary solar wind inputs used to simulation a Carrington-type event in GSM coordinates. From top to bottom are IMF B_y, IMF B_z, velocity (V_x component), density (N_p) and the temperature (Temp). The three vertical dashed red lines (A–C) show specific time instants of interest discussed further in the main text.

an excellent benchmark on which to test 3-D MHD models under extreme space weather driving conditions. We emphasize that our goal is to explore the response of the induced ground geoelectric field to such an "assumed" *Dst* of −1600 nT and not to try to exactly reproduce the Carrington event magnetogram signature or features. This is important as we attempt to investigate the maximum possible geoelectric that can be generated by extreme space weather events. So, the minimum intensity as recorded at Colaba is used as a benchmark for our modeling process, and the interplanetary conditions were particularly constructed (reverse engineered) to reproduce the peak intensity.

Figure 1 contains a 4 h time series of the constructed solar wind upstream boundary conditions, in Geocentric Solar Magnetospheric coordinates, used in the simulation. The figure displays from top to bottom: the IMF B_y component, IMF B_z component, the plasma velocity V_x component, the solar wind density (N_p), and the temperature (Temp.). We set IMF $B_x = 0$ for all simulations to keep magnetic field divergence-free condition at the inflow boundary, and also, note that other parameters (i.e., V_y and V_z), which are traditionally set to zero or some constant value, were allowed to fluctuate at a small level (10–20%). This was done for balancing the magnetosphere reaction against the strong forcing introduced by the other extreme solar wind parameters.

We note that the solar wind velocity presented in Figure 1 is not unprecedented during intense modern era CMEs. Some of the fastest CMEs on record have been observed with velocities exceeding 2000 km/s, such as the storms of October−November 2003 [*Gopalswamy et al.*, 2005a], and most recently, the 23 July 2012 event [e.g., *Russell et al.*, 2013; *Baker et al.*, 2013; *Ngwira et al.*, 2013b]. However, the IMF B_z component reveals unusually large field strengths. The strongest absolute field strengths measured at 1 AU are in the range of 65–80 nT, while here, B_z was sustained around −210 nT for about 2 h during the main phase. As pointed out by *Manchester et al.* [2006], while these field strengths are unusually high, such values are necessary to explain the large Colaba magnetic excursion associated with the Carrington event. In contrast, the IMF B_y values are fairly typical of other large storm events.

Furthermore, the maximum solar wind density exhibited here is also unusually large, providing a solar wind dynamic pressure about 4 times higher than the Halloween storm of October 2003. One of the largest observed densities on record was reported by *Burlaga et al.* [1998] for an interplanetary magnetic cloud that contained a plug of cold high-density material with an unusual density of nearly ∼180 cm^{-3} during a storm in January 1997. Considering the ground magnetic footprint of the January 1997 storm, *Li et al.* [2005] suggested that the required dynamic pressure and kinetic energy density in the flow of the Carrington storm
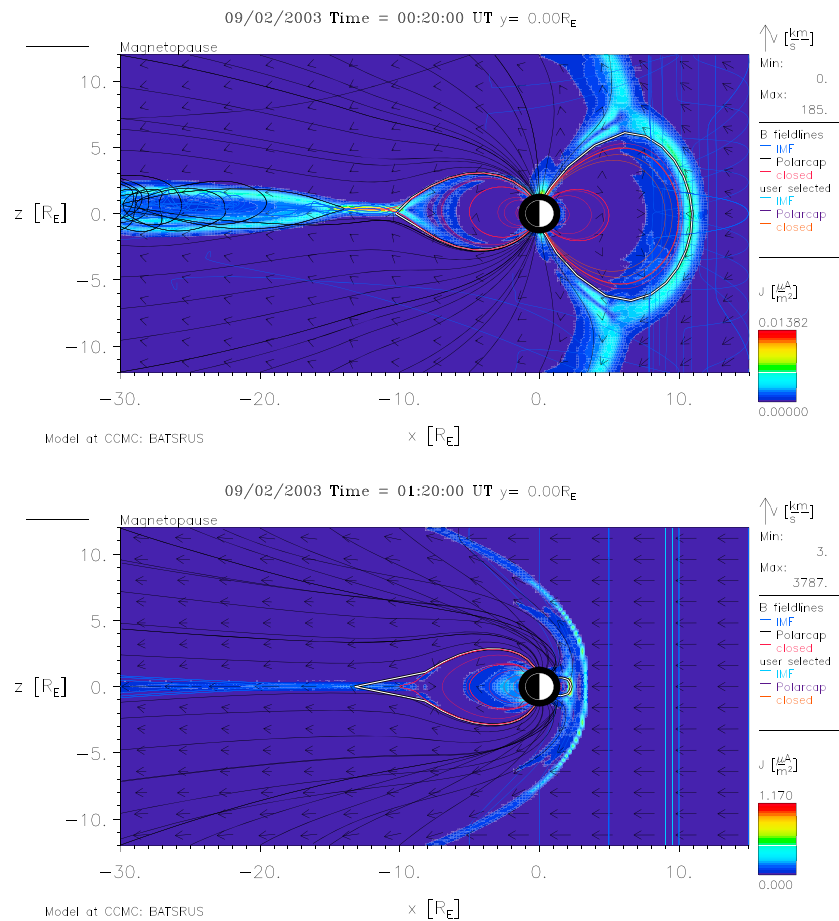
Figure 2. Simulation results of magnetosphere cut in noon-midnight meridian ($Y = 0$ plane) at two time periods during the extreme solar wind driving conditions displayed in Figure 1. The magnetosphere at (top) 00:20 UT and (bottom) at 01:20 UT, as respectively indicated by vertical lines A an B in Figure 1. Each plot also shows the current density in color, the magnetic field line traces and the solar wind flow represented by arrows. The white trace shows the boundary between the open and closed field lines. Note that the color coding is different between the two panels.

could have been about 100 times larger and thus used this as a justification for the extremely large density they used in their study. However, as demonstrated in Figure 1, we used a density about two and half times larger than that reported by *Burlaga et al.* [1998] as a more realistic estimate of extreme solar wind density conditions. This density is much smaller (one fourth) than that reported by *Li et al.* [2005], and nearly half the value reported by *Manchester et al.* [2006]. It is argued by *Ridley et al.* [2006] that while such large densities may be too large for a typical CME, this merely makes the CME highly extreme.

It is pointed out that the artificial solar wind increase between 00:30 and 01:00 UT is probably unrealistic because of gradual change in the parameters that do not indicate existence of an interplanetary shock that must be associated with Carrington-type extreme CME events. The model could not handle such intense shock. Further work is needed to find models and/or model configurations that can handle extreme shocks. However, our main interest is to study the storm main phase dynamics and not the magnetosphere response to the shock transient. Therefore, the shock is not the primary concern for this specific study. Nevertheless, this is an ongoing study and new simulation runs will be conducted to investigate the response of the magnetosphere to the solar wind shock transient.

4. Simulation Results and Interpretations

4.1. Magnetospheric Response

Figure 2 shows examples of the magnetosphere configuration in the $Y = 0$ plane at two different time periods. Also, here the IMF B_z component controls the global magnetospheric configuration. Figure 2 (top) shows the steady state period when B_z varies between −6 and 7 nT; thus, the global magnetospheric
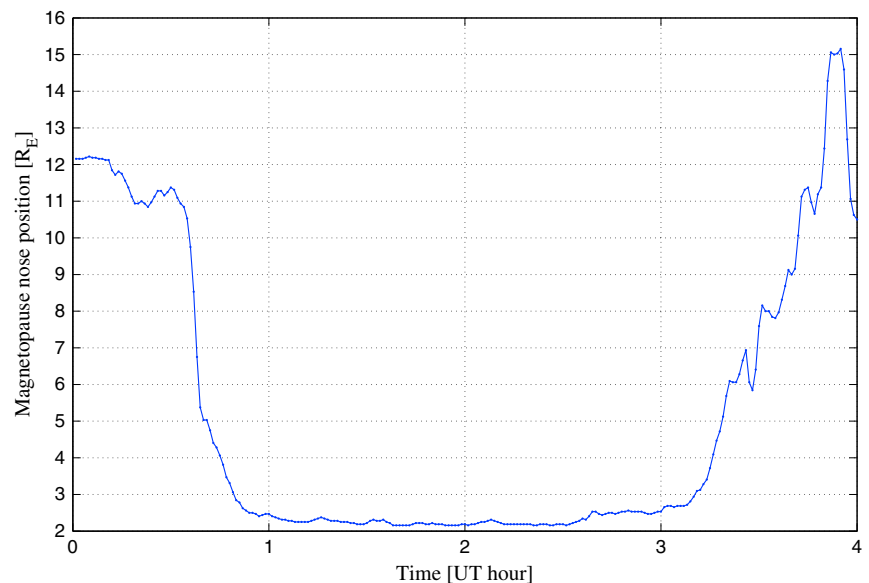
Figure 3. Simulated magnetopause standoff distance for the solar wind conditions in Figure 1. The magnetopause stand-off distance is the distance of the last closed field line of the magnetosphere measured from the center of the Earth along the GSM Sun-Earth line.

configuration never switches to pure "South" or "North" configuration. However, in Figure 2 (bottom) the magnetosphere dramatically changes during the main phase when B_z becomes dominantly southward, and the associated current systems both in the magnetosphere and ionosphere are also enhanced. At the same time, the solar wind dynamic pressure greatly increases, and the dayside magnetosphere is dramatically pushed earthward to about 2.5 R_E. The solar wind dynamic pressure and the IMF primarily control the shape and location of the Earth's magnetopause. The magnetopause current density (color coded, which is different between the panels) significantly increased as the magnetopause was pushed inside geosynchronous orbit (to ∼ 2.3 R_E, as seen in Figure 3) due to the strong compression during the pressure enhancement. The magnetopause location relative to geosynchronous orbit has important space weather implications because when the magnetopause moves past geosynchronous orbit, satellites at that location are exposed to solar wind plasma conditions in the magnetosheath.

The plasma pressure in the inner magnetosphere plays a key role in plasma dynamics and generation of electric currents. A stronger magnetotail pressure is believed to contribute to presence of large region 2 Birkeland currents that shield the inner magnetosphere from the dawn-dusk convection electric field [*De Zeeuw et al.*, 2004]. In the BATSRUS code, the pressure peak is less diffuse and increases the current flows into the ionosphere, thereby allows for the formation of much stronger region 2 currents. Figure 4 displays the inner magnetosphere pressure for two specific cross sections. In Figure 4a there is a high inner magnetosphere pressure created in the night sector compared to the dayside as computed by the BATSRUS, whereas Figure 4b shows that the high-pressure region is also shift toward the premidnight sector. Typical inner magnetosphere plasma pressure for moderate geomagnetic storms, i.e., *Dst* ∼250 nT, can be around 300 nPa [e.g., *Ebihara et al.*, 2004], which is far less than the pressure of around 6000 nPa produced in the present simulation. This large pressure in the simulation helps to explain the development of a complex region 2 FACs distribution and a much stronger ring current that are discussed in the next two sections.

4.2. Ionospheric Response
In SWMF the ionospheric potential is derived from the FACs generated by the MHD solution and an ionospheric conductance pattern. FACs play a vital role in the solar wind-magnetosphere-ionosphere interaction by electrodynamically connecting magnetospheric and ionospheric plasmas, so that stresses applied to the outer magnetosphere plasma are propagated to the ionosphere and consequently to the upper atmosphere. This is especially important during periods of large magnetospheric stress as exerted by reconnection at the dayside magnetopause and by internal processes such as geomagnetic storms and substorms. Samples of the simulated electric potential (top) and FAC (bottom) are shown in Figure 5 at an
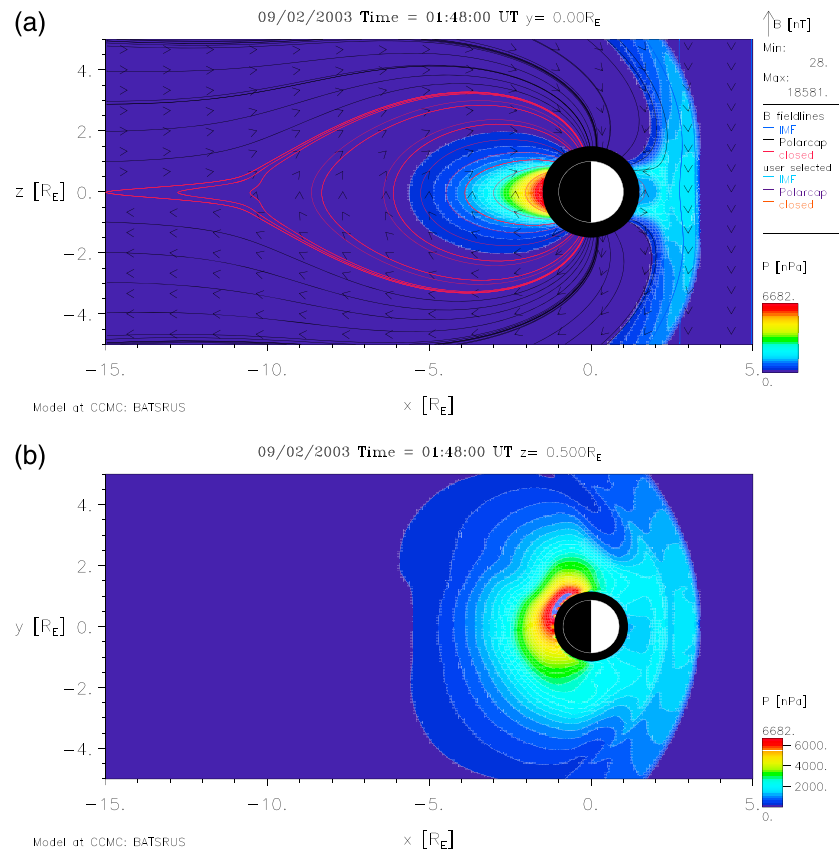
Figure 4. (a) Plot of pressure (in nPa) and magnetic field line (B_x) in the $Y = 0$ plane at different times during the simulated event. The pressure is in color and the magnetic fields represented by traced lines. (b) Pressure in the $Z = 0.5 R_E$ plane.

instance of strong driving conditions. Generally, the simulation results yield substantially larger ionospheric potentials in comparison to published values determined for previously observed events, with a peak potential value around 975 kV, while the FACs also reveal significant region 1 current with a distorted or broken up region 2 current system.

Looking further at Figure 5 (bottom), region 1 currents are quite large and considerably displaced to much lower latitudes (low L values) on the dayside than observed before. Region 1 currents, which generally appear at polar latitudes, are directly controlled by conditions in the solar wind and the IMF driving of the magnetosphere [*Ridley et al.*, 2004]. Thus, given the extreme nature of the solar wind conditions here, we expect increased continuous magnetic reconnection activity on the dayside magnetosphere [*Kuznetsova et al.*, 2007] to generate intense region 1 currents. Intense levels of southward IMF B_z lead to more efficient reconnection over an extended magnetic region, while the large solar wind density and speed bring more magnetosheath particles into the polar cusp. The open-closed field line boundary location maps to the magnetosheath and is determined by magnetic reconnection rate [e.g., *Johnsen and Lorentzen*, 2012, and references therein]. According to *Johnsen and Lorentzen* [2012], during southward IMF, which favors reconnection on the subsolar magnetopause, reconnection erodes the Earth's magnetic field moving the reconnection X line closer toward the Earth and consequently pushing the dayside open-closed boundary equatorward. *Zhang et al.* [2005] argue that there are two factors that might shift the open-closed boundary on the dayside to lower latitudes: (1) a sufficiently large ring current in the nightside during a large southward IMF tends to reduce the Earth's magnetic field in the dayside, and (2) the dayside high-latitude magnetic fields compressed by the solar wind plasmas. As is evident from our results, the solar wind IMF B_z and density and the model-derived ring current are much larger than ever observed and may help to explain the substantial shift of the region 1 current and the open-closed boundary on the dayside.
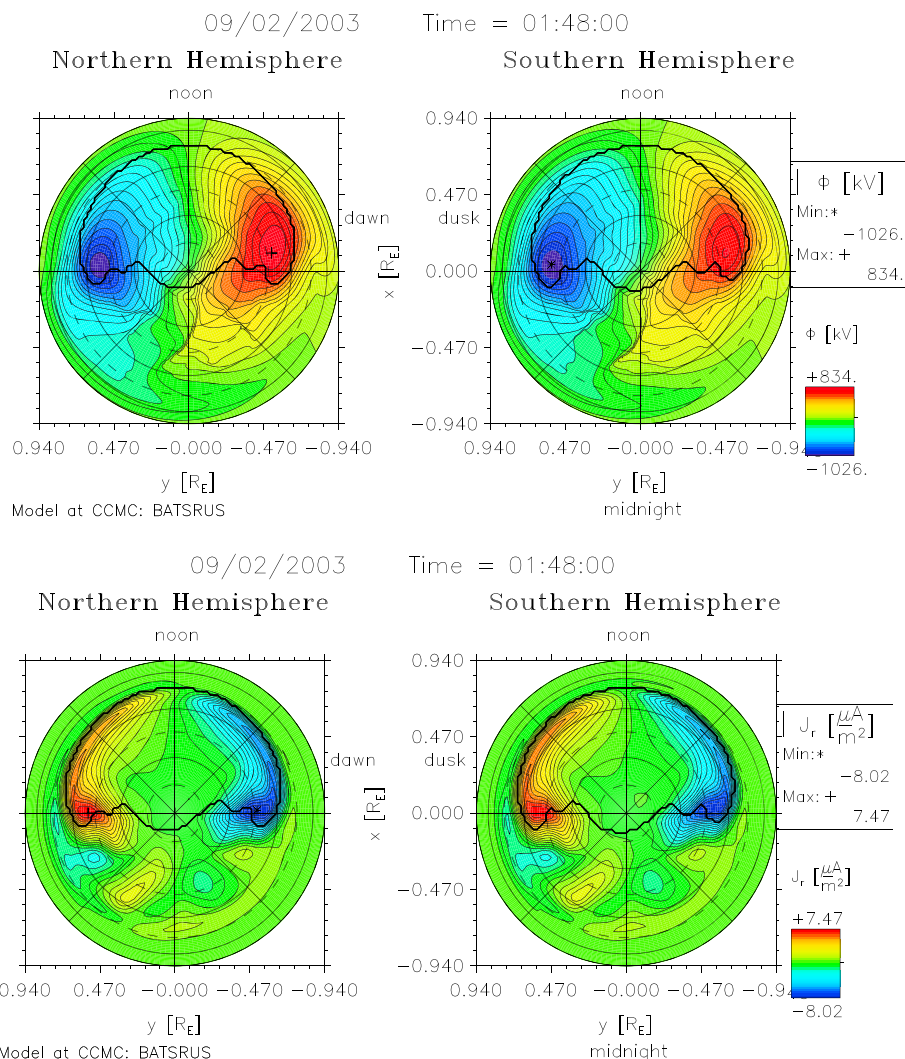
Figure 5. (top) The ionospheric electrical potential and (bottom) the field-aligned currents derived from the MHD model for the time instance indicated by vertical line C in Figure 1. The North and South magnetic poles are at the centers, respectively. For each plot, the geomagnetic pole is at the center and the outer circle is 20° geomagnetic latitude. The solid black trace shows the polar cap boundary location.

On the other hand, region 2 currents that are generally equatorward of region 1 currents appear distorted in nature with relatively smaller intensity than region 1 currents, as exhibited in Figure 5 (bottom). The region 2 FACs not only appear at much lower latitudes but in this case are also shifted more to the premidnight sector. Region 2 currents are produced by pressure gradients in the inner magnetosphere [*Toffoletto et al.*, 2003]; hence, the location of the region 2 currents is consistent with the high-pressure (see Figure 4) areas in the inner magnetosphere that map into the ionosphere. *Chun and Russell* [1997] investigated the geomagnetic control of FACs in the inner magnetosphere and found that at the highest levels of geomagnetic activity, the region of FACs expanded and was seen with greater frequency at lower *L* values throughout most local times, particularly in the premidnight and postmidnight sectors. A close relationship exists between the ring current and region 2 FACs, which is regulated by solar wind and by ionospheric conditions. The detailed mechanisms associated with this complicated ("broken up" appearance) nightside FAC distribution from MHD solution are still unknown and will need to be further explored. However, *Ebihara et al.* [2005] studied the ring current and magnetosphere-ionosphere coupling during the 20 November 2003 superstorm and found that the equatorward edge of the region 2 FAC moved to much lower latitudes and developed a complicated distribution pattern. They associated this to changes in the convection electric
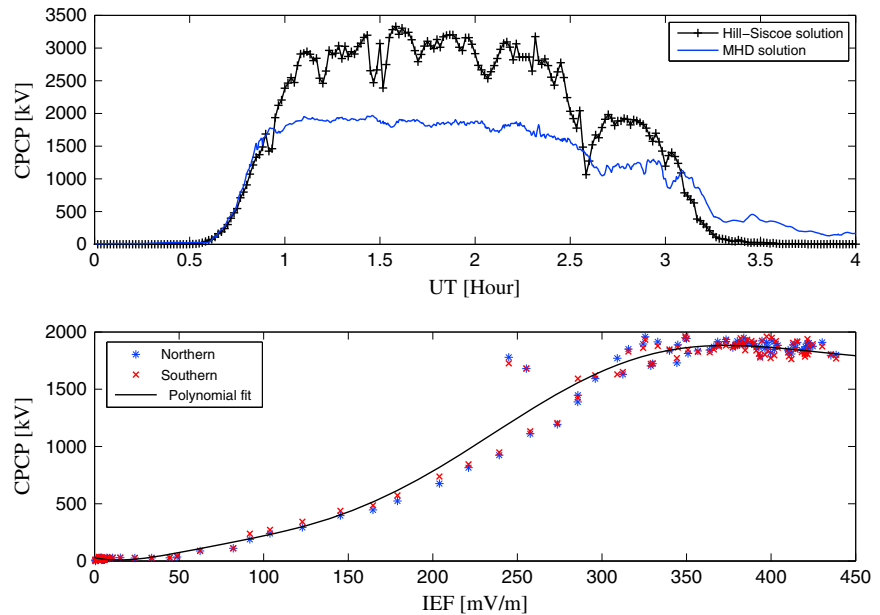
Figure 6. (top) The MHD solution ionospheric Northern cross polar cap potential as a function of time. An overlay of the Hill-Siscoe formulation of the CPCP according to *Siscoe et al.* [2002] is also shown. (bottom) The ionospheric Northern and Southern cross polar cap potential as a function of IEF $= V_x \times B_t$, where $B_t = (B_y^2 + B_z^2)^{1/2}$ is the IMF transverse component.

field and changes in the plasma sheet density that relate to changes in the plasma pressure distribution in the magnetosphere.

Figure 6 (top) contains the ionospheric cross polar cap potential (CPCP) for this simulation with an overlay of the Hill-Siscoe formulated CPCP [*Siscoe et al.*, 2002; *Shepherd et al.*, 2003]. Figure 6 (bottom) clearly shows that the well-known transpolar potential relationship between the CPCP and the interplanetary electric field is followed by both models. However, the CPCP values are much higher than normally observed; therefore, saturation occurs at substantially elevated levels. Observations, theory, and modeling indicate that typical peak CPCP values for previously observed severe geomagnetic events range between 150 and 500 kV [e.g., *Siscoe et al.*, 2002; *Kivelson and Ridley*, 2008; *Wilder et al.*, 2011, and references therein]. The much elevated CPCP values here can be attributed to the extremely large solar wind density [see, e.g., *Ridley et al.*, 2006]. Also, the large ionospheric potentials are related to the large IMF B_z driving conditions shown here to vary between −150 and −230 nT, as the electric potential is also a function of the IMF and the clock angle from the north [e.g., *Fedder et al.*, 1998; *Ridley et al.*, 1998]. We are of the view that the extreme B_z component coupled with other factors, such as extreme solar wind density and resulting high tail pressure, explains the overall large FAC strength in the MHD solution.

Generally, magnetosphere-ionosphere coupling in global MHD simulations is implemented by processes in which the magnetosphere furnishes the ionosphere with FACs that control the electric potential distribution in the ionosphere, and a feedback of electric fields from the ionosphere to the magnetosphere in order to drive magnetospheric convection [*De Zeeuw et al.*, 2004]. It is well known that ionospheric conductance plays a central role in all these processes by controlling the ionospheric electrostatic state [see, e.g., *Fuller-Rowell and Evans*, 1987; *Ridley et al.*, 2004]. Displayed in Figure 7 are the Pedersen and Hall conductance for the same day and time period as the MHD results shown in Figures 4 and 5. In the nightside ionosphere, the Hall and Pedersen conductivities also exhibit very complex structures that might be related to the FAC distributions. This is not surprising since the conductivities in the MHD solution are dependent on the FACs [*Ridley et al.*, 2004]. More detailed investigations need to be carried out to understand the development of the complex FACs and conductivity distributions.

The simulation results also show that the polar cap shifts substantially toward the dayside, extending to about ±20° of geomagnetic latitude at its maximum expansion stage, as illustrated in Figure 8. This figure depicts the ionospheric current density at two specific time periods of the simulation, that is, at 00:20 UT
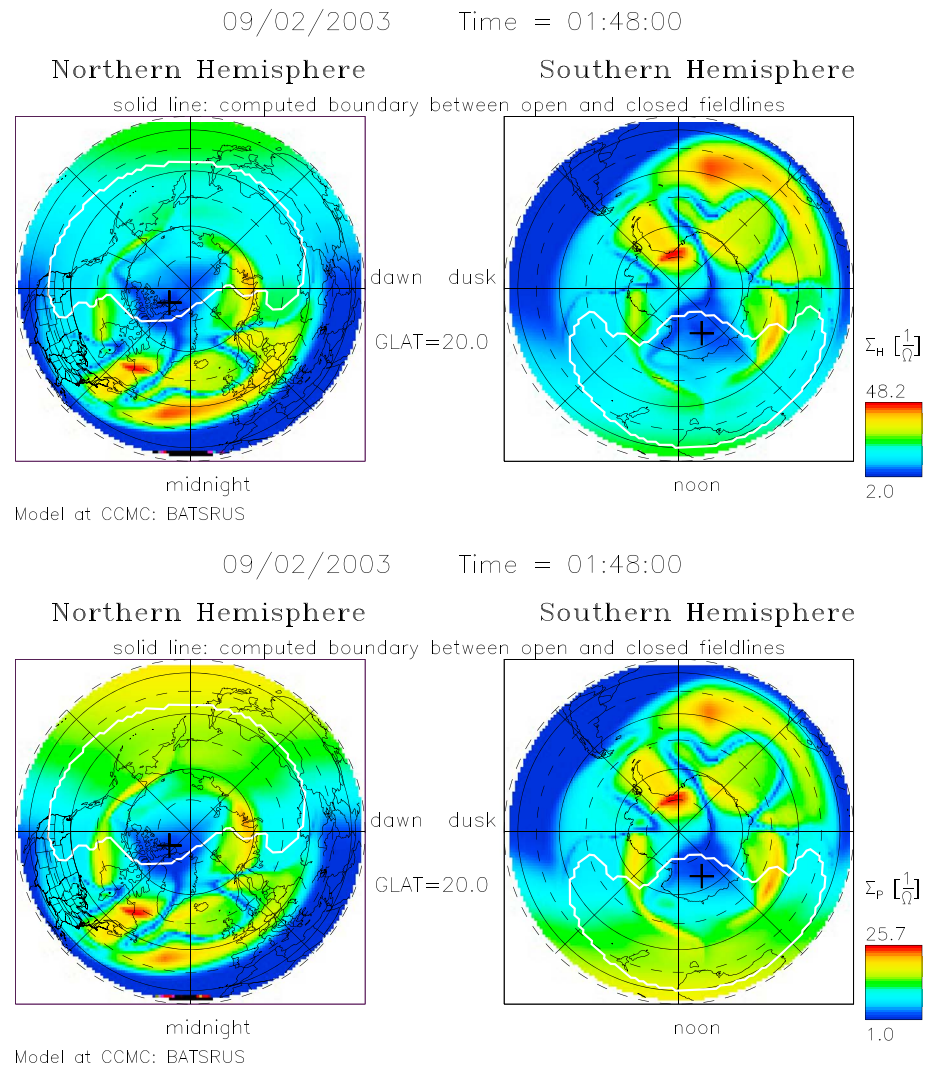
Figure 7. The ionospheric (top) Hall and (bottom) Pedersen conductance, plotted in the same manner as parameters in Figure 5. The solid white trace shows the polar cap boundary location.

(Figure 8, top) and 01:20 UT (Figure 8, bottom), and the thick white trace defines the simulated polar cap boundary location, with an underlying map depicting the geographic continents. During severe geomagnetic storm events, the polar cap boundary is known to move equatorward into the higher midlatitudes. However, significant shifting/expansion of the polar cap, as shown in our simulation, can bring auroral ionospheric currents to even much lower latitudes and also allow access for energetic particles precipitating from space into the atmosphere to lower than normal geomagnetic latitudes. The increased radiation, which could be located in previously unanticipated regions, can be harmful to the crew and passengers of flights going through the significantly shifted polar cap environment cite (see report by *Copeland* [2005]), and can also adversely affect HF radio wave propagation in these regions [see, e.g., *Goodman*, 2005]. In addition, there is a clearly manifested asymmetry in the polar cap shift between the winter and summer hemispheres (about 10°), with a greater shift observed in the Southern Hemisphere. This asymmetry can be explained by either the seasonal variation in the ionospheric Pedersen conductance [e.g., *Fedder et al.*, 1998; *Ridley et al.*, 2004] or the dipole tilt angle, which favors more reconnection between the IMF and the summer magnetosphere than the winter magnetosphere [e.g., *Wang et al.*, 2008].

4.3. Geomagnetic and Geoelectric Field Response
In the present study, the ring current strength is estimated using the geomagnetic *SYM-H* index [*Wanliss and Showalter*, 2006], a high-resolution equivalent of the *Dst* index computed at 15 s interval in our modeling.
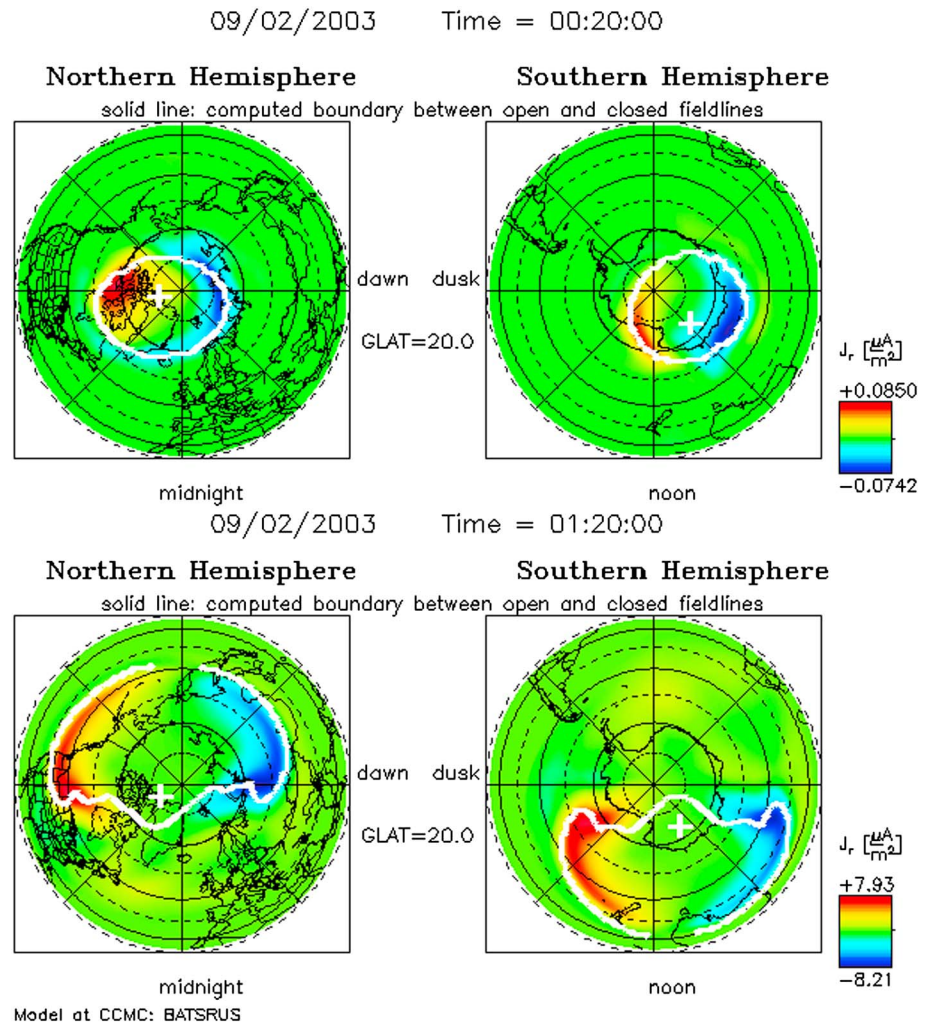
Figure 8. Ionospheric current density at two specific time periods of the simulation, that is, (top) 0020 UT and (bottom) 0120 UT. The thick white line depicts the polar cap boundary location, while the underlying map shows the geographic continents.

Depicted in Figure 9 is the geomagnetic *SYM-H* index (thick black trace) and selected examples (color) of low-latitude horizontal geomagnetic field perturbations derived from the MHD model. As is seen from Figure 9, the modeled *SYM-H* and the low-latitude geomagnetic perturbation levels are comparable to the estimated Colaba magnetogram magnetic field perturbation of about −1600 nT. An intensified ring current can be related to enhanced magnetospheric convection [e.g., *Kataoka et al.*, 2005], which is approximately proportional to the enhanced CPCP, that forces the protons from the nightside plasma sheet deeper into the inner magnetosphere. There has been a wide debate between those who argue that the Colaba Observatory magnetogram recording represented the *Dst* or the magnetospheric currents and those who believe that ionospheric currents constitute a major portion of the recording [see *Tsurutani et al.*, 2003; *Siscoe et al.*, 2006; *Cliver and Dietrich*, 2013, and references therein]. This question about different electric current sources contributing to the Colaba recordings is not addressed in this paper but is a subject we are actively pursuing in the follow-up investigation. As we stated earlier, the ultimate goal of the current paper is to explore the level of geoelectric fields that can be induced by a storm of extreme magnitude, i.e., $Dst \approx 1600$ nT.

Then, we use the SWMF-generated ground magnetic perturbations as our primary data for modeling the global induced ground geoelectric field distribution. Figure 10 displays example time series of induced ground geoelectric field components and magnetic perturbations at two active International Real-time Magnetic Observatory Network (INTERMAGNET) sites, i.e., Ottawa (55.43°N, 355.6°W, geomagnetic) in North
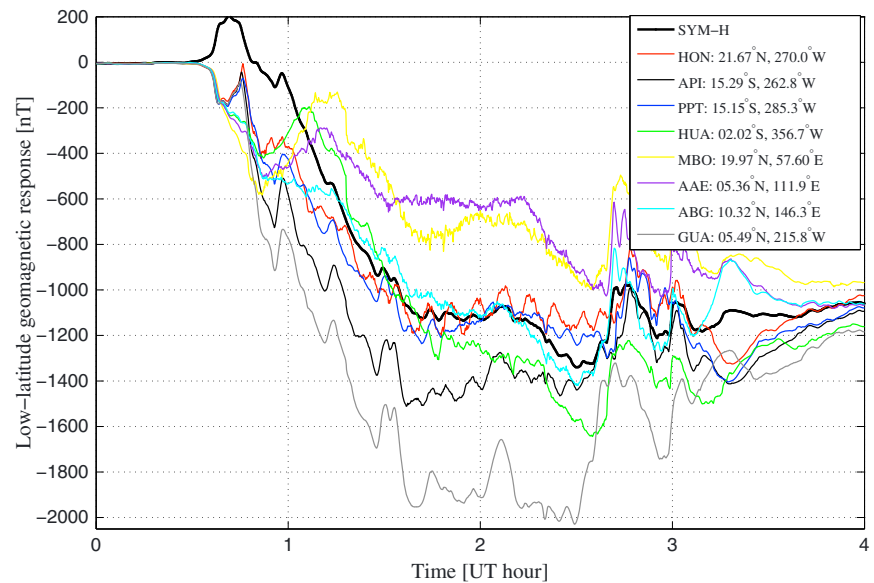
Figure 9. (The MHD model computed geomagnetic *SYM-H* index (*Dst*) and low-latitude horizontal geomagnetic field perturbations using the solar wind parameters in Figure 1. The ground locations (with geomagnetic coordinates) presented in this plot are displayed in the legend.

America and Eskdalemuir (57.74°N, 83.62°E, geomagnetic) in the European sector. The figure shows that the time of the maximum electric fields occurred during different time periods at each site.

Figure 11 shows the distribution of global maximum induced ground geoelectric fields determined for all INTERMAGNET sites. Simulation results for the Carrington-type event are displayed in Figure 11a. It is clearly evident from the figure that the model is able to reproduce the global geoelectric field distribution as described in-depth by *Pulkkinen et al.* [2012] and more recently by *Ngwira et al.* [2013a]. To further test the MHD model performance, a simulation of a portion of the Halloween superstorm on 29 October 2003 was carried out using the same model settings. Then, we compared the maximum geoelectric field determined from the model-derived geomagnetic perturbations to the geoelectric field computed from observed geomagnetic field variations for the same portion of the storm event. Results are provided in Figure 11b showing a comparison for the Halloween storm of the geoelectric field determined from model-derived geomagnetic perturbations (blue) and the geoelectric field determined from observations (red) with a very good agreement. This gives us confidence in the MHD code performance and the results since the model is generally able to capture the characteristic global geoelectric field distribution pattern. However, it is noted from Figure 11b that the geoelectric fields determined from the model-derived geomagnetic perturbations are underestimated at the auroral zones by up to 40% when compared to values computed from the observations. Consequently, we argue that the geoelectric field values at the auroral zones for the Carrington-type event may actually be larger than depicted.

Pulkkinen et al. [2007] investigated induced ground geoelectric fields and currents generated from upstream solar wind to the surface of the Earth using first-principles modeling. They observed that despite the success in reproducing some of the observed features of the GIC-related ionospheric current variations, the $3 R_E$ inner magnetospheric boundary of the global MHD setup did not extend very low in magnetic latitude in the ionosphere. This was considered as a major shortcoming during extreme geomagnetic storms because the auroral oval with highly varying ionospheric currents that generate large GIC could expand below the ionospheric MHD boundary. The aforementioned shortcoming is not an issue here because the inner magnetosphere boundary is set much closer to Earth for our simulations. *Pulkkinen et al.* [2007] further go on to emphasize that realistic modeling of the ionospheric currents is perhaps the most vital factor that contributes to the accuracy of the computed induced fields. Therefore capturing as many central physical elements as possible that contribute to the magnetosphere-ionosphere coupling is very important. However, it is obvious that some physics may be missing partially or altogether in the MHD based description of the system, thus the current standard single fluid MHD code does not fully capture the dynamic
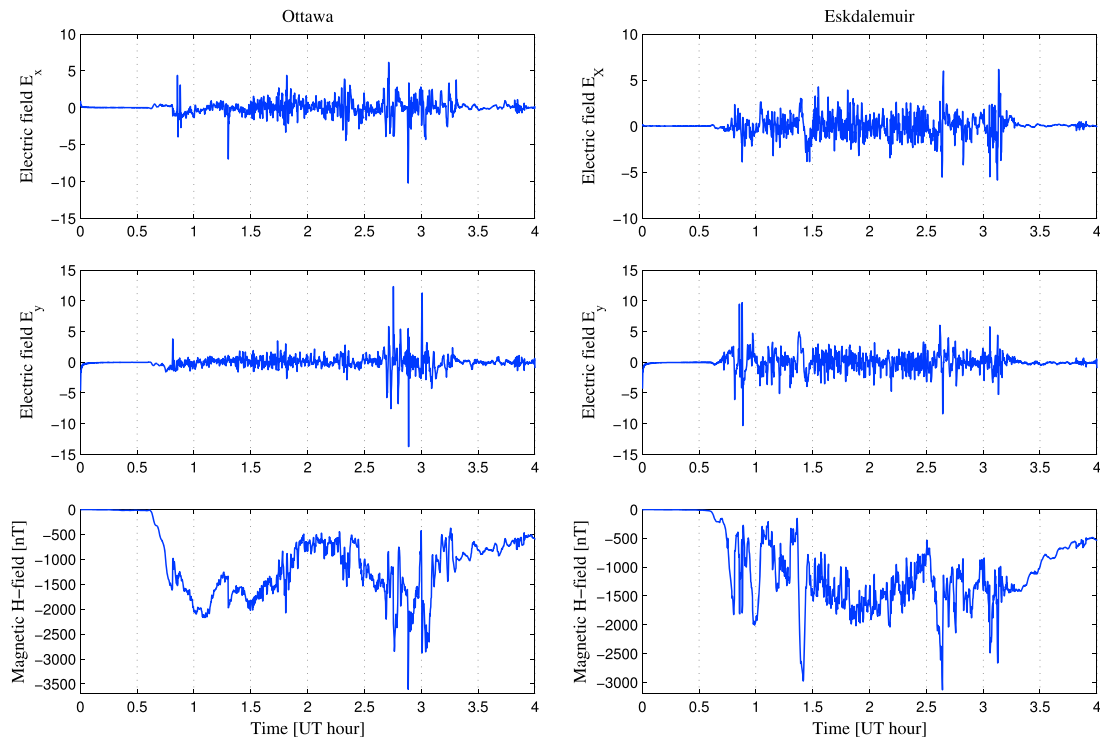
Figure 10. Example simulated time series of induced ground geoelectric field components E_x (top) and E_y (middle). The bottom panels show the simulated time series of the horizontal ground magnetic field perturbations. The two selected high-latitude magnetometer locations are Ottawa (left) and Eskdalemuir (right).
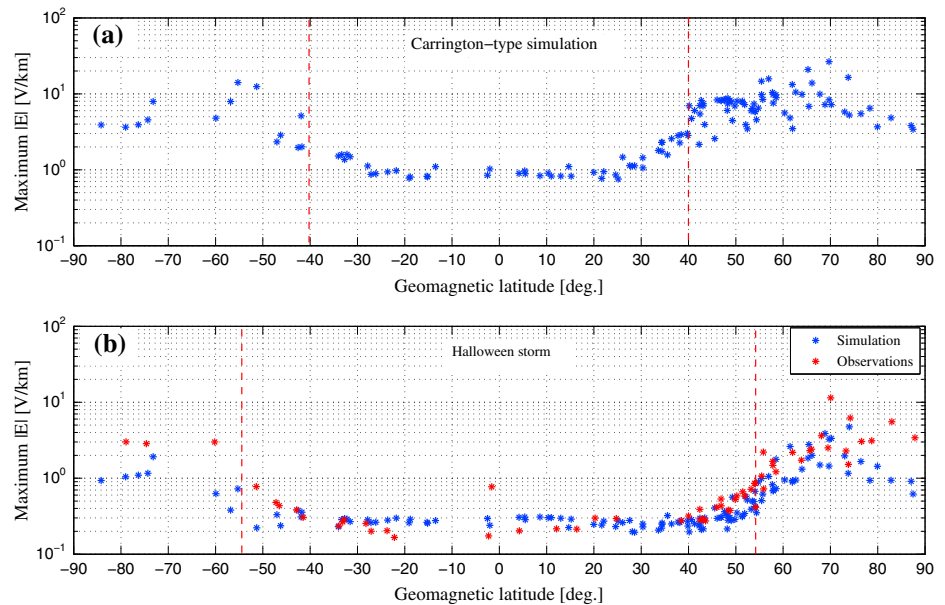

Figure 11. Global distribution of the peak geoelectric fields determined for (a) the Carrington-type event simulation, and (b) for the Halloween storm event, i.e., simulation in blue and observations in red. Each '*' represents a specific ground magnetometer site, and the time of the peak electric field varies from site-to-site. The vertical red dashed lines show the locations of the transition regions between middle and high latitudes, and are described in-depth by *Pulkkinen et al.* [2012] and more recently by *Ngwira et al.* [2013a].
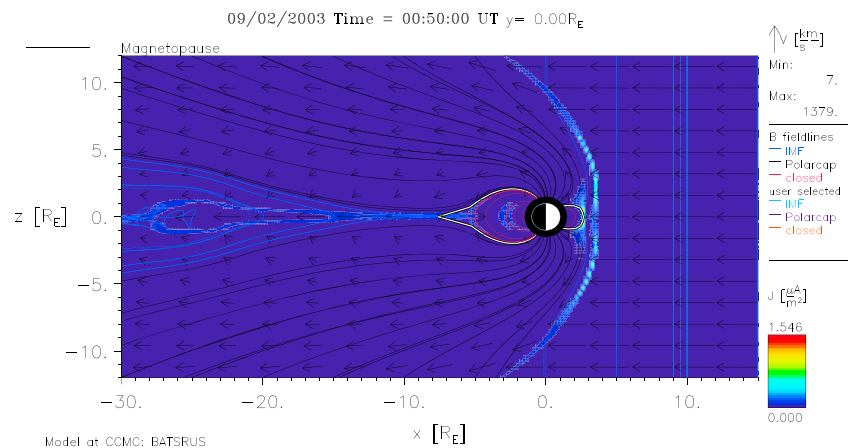
Figure 12. Magnetosphere cross section showing evidence of a plasmoid feature in the magnetotail region between $X = [-15, -7]$ R_E and $Z = [-5, 5]$ R_E. The plot shows the current density, J, in color; solar wind velocity, V_x, arrows; and magnetic field, B_x, field line traces. The IMF and magnetic field line traces can be system defined (B field lines) or user selected. The white trace shows the boundary of the last closed field line.

processes which drive large substorm current systems, as illustrated in the example event above. For instance, it is widely recognized that some processes in the plasma sheet are beyond the scope of MHD [e.g, *Glocer et al.*, 2009]. These processes may play a fundamental role in certain dynamic processes such as substorm current systems.

Furthermore, Figure 11a also clearly shows that the location of the geomagnetic latitude boundary, which is the transition region between the middle and high latitude likely caused by the auroral electrojet current, shifted to ~40° geomagnetic latitude. This geomagnetic location of the geomagnetic latitude boundary is consistent with the location of the open-closed field line boundary discussed earlier above, which is related to the auroral oval [*Zhang et al.*, 2005]. The equatorward displacement of the geomagnetic latitude boundary is much lower than previously determined (50-55° geomagnetic) for observed severe geomagnetic storm events [see reports by *Pulkkinen et al.*, 2012; *Ngwira et al.*, 2013a]. Noteworthy equatorward expansion of the auroral electric current system has important practical applications for power transmission grid operations in that power systems that were previously considered not to be subject to the auroral electric current system could be exposed to much larger levels of electric currents with the potential to drive large-amplitude GIC, thereby increasing their susceptibility to GIC risks. It is important to emphasize here that a power system's response to geomagnetic disturbances is governed by several factors, and the geoelectric field amplitude is only one part of the full power system impact analysis.

Evidence is provided in Figure 12 suggesting that the large simulated geoelectric fields are driven by magnetospheric substorm activity, as simulated plasmoid features are manifested in the magnetotail during the strong solar wind driving period. Plasmoids, which are associated with substorm onset, are large magnetic structures that are formed by separating closed plasma sheet field lines in the near-Earth magnetotail through magnetic reconnection [e.g., *Moldwin and Hughes*, 1993; *Baker et al.*, 1996]. As the plasmoid grows, a magnetic neutral point forms in the near-Earth region, then the plasmoid is pushed tailward at high speeds, and some amount of plasma is accelerated toward the Earth, causing intensification of the auroral current at Earth's high-latitude nightside and accompanying geomagnetic disturbance [e.g., *Baker et al.*, 1996]. The nightside region 2 FACs and their expansion to much lower L values could be related to substorms and the substorm current wedge (SCW). The SCW is a vital feature of the substorm expansion phase formed by the dipolarization of the nightside magnetotail and intensification of the westward electrojet following auroral substorm onset [*Murphy et al.*, 2013, and references therein]. Studying the detailed spatial structure of FACs in the SCW, *Murphy et al.* [2013] demonstrated that the FACs formed from the SCW exhibited evidence of small-scale FAC structures and was more complex than the standard equivalent current system of the SCW. In addition, these authors discovered that in the premidnight sector, a more complicated current system was generated following substorm onset with no evidence of the distinct region 1 and region 2 current systems as reported in earlier investigations such as *Iijima and Potemra* [1978]. It therefore
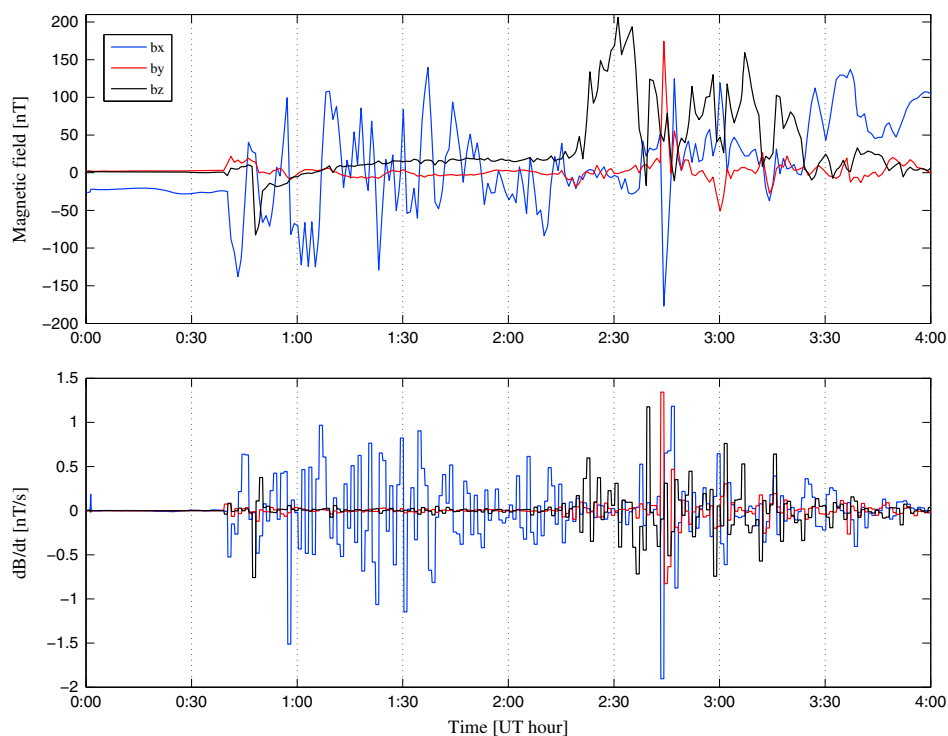
Figure 13. (top) The model geomagnetic field generate in the simulation for a virtual satellite at a specific location in the magnetotail, i.e., $X = -15\ R_E$, $Y = 0$ and $Z = 0$. (bottom) The respective rates-of-change components, dB/dt. The largest dB/dt values (i.e., around 00:30–01:00 and 02:30–03:00 UT) are consistent with peak geoelectric fields displayed in Figure 10.

seems that this complex FAC distribution can develop under extreme geomagnetic conditions, and needs to be investigated in greater detail.

Finally, the illustration in Figure 13 contains the geomagnetic field components (top) and the respective rates of change (bottom), dB/dt, for a selected location within the plasmoid feature in the magnetotail. The figure demonstrates that there are sharp changes in some of the magnetospheric magnetic field components at about 00:51 UT and 02:45 UT for the specified location. These are roughly the same times that plasmoid features are released in the tail region. Perturbations in the magnetotail magnetic fields are related to traveling compression regions reflecting the motion of the plasmoid which forces the lobe magnetic field lines to compress around it [*Draper et al.*, 2005]. The corresponding rate-of-change components from Figure 13b show rapid variations at the same instances as the magnetic field components. As seen, these are the most significant changes during the disturbed period and can be related to the large changes in the geoelectric field on the ground at the above mentioned time periods displayed in Figure 10. Statistically, substorms are acknowledged to be one of the most effective causes for large high-latitude GIC [e.g., *Viljanen et al.*, 2006].

5. Summary and Conclusions

In the present paper we use a 3-D MHD model with specially refined components for modeling extreme space weather events. The core MHD model is based on the University of Michigan SWMF that uses the BATSRUS code to predicts in a self-consistent manner the dynamic response of the large-scale magnetosphere to changing solar wind conditions. Our ultimate future goal is to apply this model to simulating GIC events under extreme solar wind conditions.

We have shown the magnetospheric, ionospheric and ground response to extremely large Carrington-type solar wind driving conditions. During the idealized extreme CME, the magnetosphere is compressed considerably with the magnetopause seen to move way inside of geosynchronous orbit ($\sim$2.3 R_E). There is a strong

dawn-dusk inner magnetosphere pressure asymmetry with the average pressures on the nightside much greater than that on the dayside leading to large region 2 FACs.

In the ionosphere, the CME drives large and complicated region 1 and region 2 field-aligned current distributions, leading to extremely large ionospheric potentials. We believe that the nightside complex region 2 FACs and their appearance at lower L values are related to substorms and the substorm current wedge, as we see evidence of magnetic field lines stretching and snapping in the tail region around the same time. Interestingly, the polar cap is subject to a dramatic displacement reaching about 20° geomagnetic latitude. The polar cap displacement is also important to take into account for airline companies operating transpolar flights because it can endanger airline crews and passengers, and can cause polar cap absorption events, which adversely affect radio wave propagation leading to complete HF radio blackout. Therefore, under extreme forcing from the solar wind, absorption events can exist in regions previously considered to be unaffected by such phenomenon.

On the ground, the CME generated very strong geomagnetic perturbations which lead to large calculated global geoelectric fields. These high levels of geoelectric fields in turn have the potential to drive large GIC in ground conductors such as power grids and oil pipelines. In addition, the maximum high-latitude geoelectric field of 26 V/km presented in Figure 11a for the Carrington-type event is comparable to predicted theoretical maximum for the 100 year scenario (20 V/km) reported by *Pulkkinen et al.* [2012]. Consequently, a Carrington-type event poses an enhanced risk for grid operators because it has the potential to produce geomagnetically induced electric fields more than twice as large as those produced by previously observed Earth-directed extreme events such as the March 1989 storm (~6 V/km) or the Halloween 2003 storms (~12 V/km) [see, e.g., *Pulkkinen et al.*, 2012; *Ngwira et al.*, 2013a]. Furthermore, the strongly shifted geomagnetic latitude boundary implies that the region of large induced ground electric fields is displaced further equatorward due to a shift of the auroral current system, thereby may affect power grids in regions normally far away from the auroral zone, such as southern states of continental U.S. or central and southern Europe.

References

Baker, D. N., T. I. Pulkkinen, V. Angelopoulos, W. Baumjohann, and R. L. McPherrron (1996), Neutral line model of substorm: Past results and present view, *J. Geophys. Res.*, *101*(A6), 12,975–13,010, doi:10.1029/95JA03753.

Baker, D. N., X. Li, A. Pulkkinen, C. M. Ngwira, M. L. Mays, A. B. Galvin, and K. D. C. Simunac (2013), A major solar eruptive event in July 2012: Defining extreme space weather scenarios, *Space Weather*, *11*, 1–7, doi:10.1002/swe.20097.

Burlaga, L., et al. (1998), A magnetic cloud containing prominence material: January 1997, *J. Geophys. Res.*, *103*(A1), 277–285.

Cagniard, L. (1953), Basic theory of the magneto-telluric methods of geophysical prospecting, *Geophysics*, *18*(3), 605–635.

Chun, F. K., and C. T. Russell (1997), Field-aligned currents in the inner magnetosphere: Control by geomagnetic activity, *J. Geophys. Res.*, *102*(A2), 226–2270.

Cliver, E. W., and W. F. Dietrich (2013), The 1859 space weather event revisited: Limits of extreme activity, *J. Space Weather Space Clim.*, *3*(A31), 15, doi:10.1051/swsc/2013053.

Copeland, K., H. H. Sauer, and W. Friendberg (2005), Solar radiation alert system, DOT/FAA/AM-05/14, Office of Aerospace Medicine, Washington, D. C.

De Zeeuw, D. L., S. Sazykin, R. A. Wolf, T. I. Gombosi, A. J. Ridley, and G. Tóth (2004), Coupling of a global MHD code and an inner magnetosphere model: Initial results, *J. Geophys. Res.*, *109*, A12219, doi:10.1029/2003JA010366.

Draper, N. C., et al. (2005), Cluster magnetotail observations of a tailward-travelling plasmoid at substorm expansion phase onset and field aligned currents in the plasma sheet boundary layer, *Ann. Geophys.*, *23*, 3667–3683.

Ebihara, Y., M.-C. Fok, R. A. Wolf, T. J. Immel, and T. E. Moore (2004), Influence of ionosphere conductivity on the ring current, *J. Geophys. Res.*, *109*, A08205, doi:10.1029/2003JA010351.

Ebihara, Y., M.-C. Fok, S. Sazykin, M. F. Thomsen, M. R. Hairston, D. S. Evans, F. J. Rich, and M. Ejiri (2005), Ring current and the magnetosphere-ionosphere coupling during the superstorm of 20 November 2003, *J. Geophys. Res.*, *110*, A09S22, doi:10.1029/2004JA010924.

Fedder, J. A., S. P. Slinker, and J. G. Lyon (1998), A comparison of global numerical simulation results to data for the January 27–28, 1992, Geospace Environment Modeling challenge event, *J. Geophys. Res.*, *103*(A7), 14,799–14,810.

Fuller-Rowell, T. J., and D. S. Evans (1987), Height-intergrated Pedersen and Hall conductivity patterns inferred from the TIROS-NOAA satellite data, *J. Geophys. Res.*, *92*(A7), 7606–7618.

Glocer, A., G. Tóth, T. I. Gombosi, J.-C. Zhang, and L. M. Kistler (2009), Multifluid block-adaptive-tree solar wind roe-type upwind scheme: Magnetospheric composition and dynamics during geomagnetic storms-Initial results, *J. Geophys. Res.*, *114*, A12203, doi:10.1029/2009JA014418.

Gombosi, T. I., D. L. De Zeeuw, C. P. T. Groth, K. G. Powell, and Q. F. Stout (2000), Multiscale MHD simulation of a coronal mass ejection and its interaction with the magnetosphere-ionosphere system, *J. Atmos. Sol. Terr. Phys.*, *62*, 1515–1525.

Goodman, J. M. (2005), Operational communication systems and relationships to the ionosphere and Space Weather, *Adv. Space Res.*, *36*(12), 2241–2252.

Gopalswamy, N., S. Yashiro, Y. Liu, G. Michalek, A. Vourlidas, M. L. Kaiser, and R. A. Howard (2005a), Coronal mass ejections and other extreme characteristics of the 2003 October-November solar eruptions, *J. Geophys. Res.*, *110*, A09S15, doi:10.1029/2004JA010958.

Gopalswamy, N., S. Yashiro, G. Michalek, H. Xie, R. P. Lepping, and R. A. Howard (2005b), Solar source of the largest geomagnetic storm of cycle 23, *Geophys. Res. Lett.*, *32*, L12S09, doi:10.1029/2004GL021639.

Groth, C. P. T., D. L. De Zeeuw, K. G. Powell, T. I. Gombosi, and Q. F. Stout (1999), A parallel solution-adaptive scheme for ideal magnetohydrodynamics, paper presented at 14th Computational Fluid Dynamics Conference, AIAA 99-3273, Norfolk, Va.

Groth, C. P. T., D. L. De Zeeuw, T. I. Gombosi, and K. G. Powell (2000), Global three-dimensional MHD simulation of a space weather event: CME formation, interplanetary propagation, and interaction with the magnetosphere, *J. Geophys. Res.*, *105*(A11), 25,053–25,078.

Iijima, T., and T. A. Potemra (1978), Large-scale characteristics of field-aligned currents associated with substorms, *J. Geophys. Res.*, *83*(A2), 599–615, doi:10.1029/JA083iA02p00599.

Johnsen, M. G., and D. A. Lorentzen (2012), A statistical analysis of the optical dayside open/closed field line boundary, *J. Geophys. Res.*, *117*, A02218, doi:10.1029/2011JA016984.

Kataoka, A., D. H. Fairfield, D. G. Sibeck, L. Rastätter, M.-C. Fok, T. Nagatsuma, and Y. Ebihara (2005), Magnetosheath variations during the storm main phase on 20 November 2003: Evidence for solar wind density control of energy transfer to the magnetosphere, *Geophys. Res. Lett.*, *32*, L21108, doi:10.1029/2005GL024495.

Kivelson, M. G., and A. J. Ridley (2008), Saturation of the polar cap potential: Inference from alfven wing arguments, *J. Geophys. Res.*, *113*, A05214, doi:10.1029/2008JA012302.

Kuznetsova, M. M., M. Hesse, L. Rastätter, A. Taktakishvili, G. Toth, D. L. De Zeeuw, A. Ridley, and T. I. Gombosi (2007), Multiscale modeling of magnetospheric reconnection, *J. Geophys. Res.*, *112*, A10210, doi:10.1029/2007JA012316.

Li, X., M. Temerin, B. T. Tsurusani, and S. Alex (2005), Modeling of 1–2 September 1859 super magnetic storm, *Adv. Space Res.*, *38*(2), 273–279, doi:10.1016/j.asr.2005.06.070.

Manchester, W. B., IV, A. J. Ridley, T. I. Gombosi, and D. L. De Zeeuw (2006), Modeling the Sun-Earth propagation of a very fast CME, *Adv. Space Res.*, *38*, 253–262.

Moldwin, M. B., and W. J. Hughes (1993), Geomagnetic substorm association of Plasmoids, *J. Geophys. Res.*, *98*, 81–88.

Murphy, K. R., I. R. Mann, I. J. Rae, C. L. Waters, H. U. Frey, A. Kale, H. J. Singer, B. J. Anderson, and H. Korth (2013), The detailed spatial structure of field-aligned currents comprising the substorm current wedge, *J. Geophys. Res. Space Physics*, *118*, 7714–7727, doi:10.1002/2013JA018979.

Nevanlinna, H. (2008), On geomagnetic variations during the August-September storms of 1859, *Adv. Space Res.*, *42*, 171–180.

Ngwira, C. M., A. Pulkkinen, F. D. Wilder, and G. Crowley (2013a), Extended study of extreme geoelectric field event scenarios for geomagnetically induced current applications, *Space Weather*, *11*, 121–131, doi:10.1002/swe.20021.

Ngwira, C. M., A. Pulkkinen, M. Leila Mays, M. M. Kuznetsova, A. B. Galvin, K. Simunac, D. N. Baker, X. Li, Y. Zheng, and A. Glocer (2013b), Simulation of the 23 July 2012 extreme space weather event: What if this extremely rare CME was Earth-directed?, *Space Weather*, *11*, 671–679, doi:10.1002/2013SW000990.

Palmroth, M., T. I. Pulkkinen, and P. Janhunen (2003), Stormtime energy transfer in global MHD simulation, *J. Geophys. Res.*, *108*(A1), 1048, doi:10.1029/2002JA009446.

Palmroth, M., P. Janhunen, T. I. Pulkkinen, and H. E. J. Koskinen (2004), Ionospheric energy input as a function of solar wind parameters: Global MHD simulation results, *Ann. Geophys.*, *22*, 549–566.

Pirjola, R. (1982), Electromagnetic induction in the Earth by a plane wave or by fields of line currents harmonic in time and space, *Geophysica*, *18*(1-2), 1–161.

Pirjola, R. (2002), Review on the calculation of the surface electric and magnetic fields and geomagnetically induced currents in ground based technological systems, *Surv. Geophys.*, *23*, 71–90.

Powell, K. G., P. L. Roe, T. J. Linde, T. I. Gombosi, and D. L. De Zeeuw (1999), A solution-adaptive upwind scheme for ideal magnetohydrodynamics, *J. Comput. Phys.*, *154*(2), 284–309, doi:10.1006/jcph.1999.6299.

Pulkkinen, A., M. Hesse, M. Kuznetsova, and L. Rastätter (2007), First-principles modeling of geomagnetically induced electromagnetic fields and currents from upstream solar wind to the surface of the Earth, *Ann. Geophys.*, *25*, 881–893.

Pulkkinen, A., M. Hesse, S. Habib, L. Van der Zel, B. Damsky, F. Policelli, D. Fugate, W. Jacobs, and E. Creamer (2009), Solar shield: Forecastng and mitigating space weather effects on high-voltage power transmission systems, *Nat. Hazards*, *53*(2), 333–345, doi:10.1007/s11069-009-9432-x.

Pulkkinen, A., et al. (2011), Geospace environment modeling 2008-2009 challenge: Ground magnetic field perturbations, *Space Weather*, *9*, S02004, doi:10.1029/2010SW000600.

Pulkkinen, A., E. Bernabeu, J. Eichner, C. Beggan, and A. W. P. Thomson (2012), Generation of 100-year geomagnetically induced current scenarios, *Space Weather*, *10*, S04003, doi:10.1029/2011SW000750.

Pulkkinen, A., et al. (2013), Community-wide validation of geospace model ground magnetic field perturbation predictions to support model transition to operations, *Space Weather*, *11*(6), 369–385, doi:10.1002/swe.20056.

Pulkkinen, T. I., M. Palmroth, P. Janhunen, H. E. J. Koskinen, D. J. McComas, and C. W. Smith (2010), Timing of changes in the solar wind energy input in relation to ionospheric response, *J. Geophys. Res.*, *115*, A00109, doi:10.1029/2010JA015764.

Ridley, A. J., G. Lu, C. R. Clauer, and V. O. Papitashvili (1998), A statistical study of the ionospheric convection response to changing interplanetary magnetic field conditions using the assimilative mapping of ionospheric electrodynamics technique, *J. Geophys. Res.*, *103*(A3), 4023–4039.

Ridley, A. J., T. I. Gombosi, and D. L. De Zeeuw (2004), Ionospheric control of the magnetosphere: Conductance, *Ann. Geophys.*, *22*, 567–584.

Ridley, A. J., D. L. De Zeeuw, W. B. Manchester, and K. C. Hansen (2006), The magnetospheric and ionospheric response to a very strong interplanetary shock and coronal mass ejection, *Adv. Space Res.*, *38*, 263–272.

Ridley, A. J., T. I. Gombosi, I. V. Sokolov, G. Tóth, and D. T. Welling (2010), Numerical considerations in simulating the global magnetosphere, *Ann. Geophys.*, *28*, 1689–1614.

Russell, C. T., et al. (2013), The very unusual interplanetary coronal mass ejection of 2012 July 23: A blast wave mediated by solar energetic particles, *Astrophys. J.*, *770*(38), 5, doi:10.1088/0004-637X/770/1/38.

Shepherd, S. G., J. M. Ruohoniemi, and R. A. Greenwald (2003), Testing the Hill model of transpolar potential with Super Dual Auroral Radar Network observations, *Geophys. Res. Lett.*, *30*(1), 1002, doi:10.1029/2002GL015426.

Siscoe, G. L., G. M. Erickson, B. U. Ö. Sonnerup, N. C. Maynard, J. A. Schoendorf, K. D. Siebert, D. R. Weimer, W. W. White, and G. R. Wilson (2002), Hill model of transpolar potential saturation: Comparisons with MHD simulations, *J. Geophys. Res.*, *107*(A6), 1075, doi:10.1029/2001JA000109.

Siscoe, G., N. U. Crooker, and C. R. Clauer (2006), Dst of the Carrington storm of 1859, *Adv. Space Res.*, *38*, 173–179, doi:10.1016/j.asr.2005.02.102.

Thomson, A. W. P., E. B. Dawson, and S. J. Reay (2011), Quantifying extreme behavior in geomagnetic activity, *Space Weather*, *9*, S10001, doi:10.1029/2011SW000696.

Toffoletto, F., S. Sazykin, R. Spiro, and R. Wolf (2003), Inner magnetospheric modeling with the Rice Convection Model, *Space Sci. Rev.*, *107*, 175–196.

Tóth, G., et al. (2005), Space weather modeling framework: A new tool for the space science community, *J. Geophys. Res.*, *110*, A12226, doi:10.1029/2005JA011126.

Tóth, G., et al. (2012), Adaptive numerical algorithms in space weather modeling, *J. Atmos. Sol. Terr. Phys.*, *231*, 870–903.

Tsurutani, B. T., W. D. Gonzalez, G. S. Lakhina, and S. Alex (2003), The extreme magnetic storm of 1-2 September 1859, *J. Geophys. Res.*, *108*(A7), 1268, doi:10.1029/2002JA009504.

Viljanen, A., E. I. Tanskanen, and A. Pulkkinen (2006), Relation between substorm characteristics and rapid temporal variations of the ground magnetic field, *Ann. Geophys.*, *24*, 725–733.

Wang, H., A. J. Ridley, and H. Lühr (2008), SWMF simulation of field-aligned currents for a varying northward and duskward IMF with nonzero dipole tilt, *Ann. Geophys.*, *26*, 1461–1477.

Wanliss, J. A., and K. M. Showalter (2006), High-resolution global storm index: Dst versus SYM-H, *J. Geophys. Res.*, *111*, A02202, doi:10.1029/2005JA011034.

Weimer, D. R. (1996), A flexible, IMF dependent model of high-latitude electric potentials having "space weather" applications, *Geophys. Res. Lett.*, *23*(18), 2549–2552.

Welling, D. T., and A. J. Ridley (2010), Validation of the SWMF magnetic field and plasma, *Space Weather*, *8*, S03002, doi:10.1029/2009SW000494.

Wilder, F. D., C. R. Clauer, J. B. H. Baker, E. P. Cousins, and M. R. Hairston (2011), The nonlinear response of the polar cap potential under southward IMF: A statistical view, *J. Geophys. Res.*, *116*, A12229, doi:10.1029/2011JA016924.

Yu, Y., A. J. Ridley, D. T. Welling, and G. Tóth (2010), Including gap region field aligned currents and magnetospheric currents in the MHD calculation of ground-based magnetic field perturbations, *J. Geophys. Res.*, *115*, A08207, doi:10.1029/2009JA014869.

Zhang, Y., C.-I. Meng, L. J. Paxton, D. Morrison, B. Wolven, H. Kil, P. Newell, S. Wing, and A. B. Christensen (2005), Far-ultraviolet signature of polar cusp during southward IMF B_z observed by TIMED/Global Ultraviolet Imager and DMSP, *J. Geophys. Res.*, *110*, A01218, doi:10.1029/2004JA010707.